Taylor & Francis
Taylor & Francis Group

Green Chemistry Letters and Reviews

ISSN: 1751-8253 (Print) 1751-7192 (Online) Journal homepage: www.tandfonline.com/journals/tgcl20

Investigation of Fe’s influence on turquoise hydrogen production enhanced by Ni nanoclusters with gamma alumina support

Ainars Knoks , Liga Grinberga , Raitis K. Sika , Liga Ignatane , Marius Urbonavicius , Simona Tuckute , Janis Kleperis , Izabela Curkovic , Danjela Kuscer & Sarunas Varnagiris

To cite this article: Ainars Knoks , Liga Grinberga , Raitis K. Sika , Liga Ignatane , Marius Urbonavicius , Simona Tuckute , Janis Kleperis , Izabela Curkovic , Danjela Kuscer & Sarunas Varnagiris (2026) Investigation of Fe’s influence on turquoise hydrogen production enhanced by Ni nanoclusters with gamma alumina support, Green Chemistry Letters and Reviews, 19:1, 2668782, DOI: 10.1080/17518253.2026.2668782

To link to this article: https://doi.org/10.1080/17518253.2026.2668782

© 2026 The Author(s). Published by Informa UK Limited, trading as Taylor & Francis Group

View supplementary material

Published online: 11 May 2026.

Submit your article to this journal

Article views: 61

View related articles

View Crossmark data

Full Terms & Conditions of access and use can be found at
https://www.tandfonline.com/action/journalInformation?journalCode=tgcl20

GREEN CHEMISTRY LETTERS AND REVIEWS
2026, VOL. 19, NO. 1, 2668782
https://doi.org/10.1080/17518253.2026.2668782

OPEN ACCESS Check for updates

Investigation of Fe's influence on turquoise hydrogen production enhanced by Ni nanoclusters with gamma alumina support

Ainars Knoks[a], Liga Grinberga[a], Raitis K. Sika[a], Liga Ignatane[a], Marius Urbonavicius[b], Simona Tuckute[b], Janis Kleperis[a*], Izabela Curkovic[c], Danjela Kuscer[c] and Sarunas Varnagiris[b]

[a]Institute of Solid State Physics, University of Latvia, Riga, Latvia; [b]Center for Hydrogen Energy Technologies, Lithuanian Energy Institute, Kaunas, Lithuania; [c]Jožef Stefan Institute, Ljubljana, Slovenia

ABSTRACT

One of the challenging aspects of implementing hydrogen is the cost and availability of hydrogen, e.g. green hydrogen is costly and inaccessible, whereas conventional grey hydrogen is associated with substantial CO_2 emissions. An intermediate solution could be turquoise hydrogen, which promises substantially lower direct cost and CO_2-imposed social cost. This work investigates nickel nanoclusters on iron co-catalyst system, supported by gamma alumina, for the catalytic degradation of methane. A novel synthesis approach is tested to examine the influence of Fe amount on reaction yields and outcomes. Varying amounts of Fe with and without Ni were tested at 700, 800, and 900 °C in a batch-type reaction. Analysis of catalysts and outcomes was carried out; it was found that the use of co-catalysts on commercial gamma alumina pyrolysis yields hydrogen at 82% at lower reaction temperatures of 700 °C and 80% at 900°C. Addition of Ni nanoclusters provide higher results than those of a single Fe catalyst. The synergistic effect of Ni-Fe catalysts exhibits improved efficiency, yielding a range of valuable nanofibrous carbon tested as pesticide sensors showing promise in extending life cycle of catalyst materials.

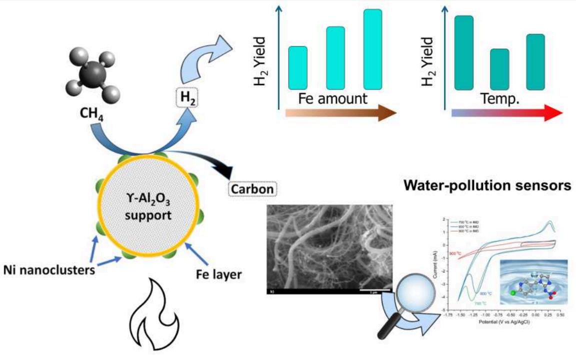

ARTICLE HISTORY
Received 9 January 2026
Accepted 29 April 2026

KEYWORDS
Iron-nickel nanoclusters; clean energy; hydrogen; pyrolysis; nanomaterials

Introduction

The importance of hydrogen energetics in the green transition is hard to overstate; it is evident that the EU has taken steps to implement large-scale hydrogen projects. This includes the generation and consumption of a substantial amount of hydrogen within the EU, as well as its export to other regions. The said course is visible due to initiatives and funding, such as the EU Clean Hydrogen Alliance (*1*), hydrogen valley platform (*2*) or the Hydrogen partnership for technologies (*3*). Even though there is a strong legislative push, hydrogen energetics face implementation limitations.

For example, in 2025, there remains a lack of infrastructure for implementing the projected green hydrogen production and storage. Currently, the industry is lagging, partly due to limited availability of specific

---

CONTACT Ainars Knoks ✉ ainars.knoks@cfi.lu.lv Institute of Solid State Physics, University of Latvia, Kengaraga street 8, LV-1063, Riga, Latvia

*The author died prior to the submission of this paper.

Supplemental data for this article can be accessed online at https://doi.org/10.1080/17518253.2026.2668782.

© 2026 The Author(s). Published by Informa UK Limited, trading as Taylor & Francis Group
This is an Open Access article distributed under the terms of the Creative Commons Attribution License (http://creativecommons.org/licenses/by/4.0/), which permits unrestricted use, distribution, and reproduction in any medium, provided the original work is properly cited. The terms on which this article has been published allow the posting of the Accepted Manuscript in a repository by the author(s) or with their consent.

technologies at affordable prices. To a broader extent, the lag is caused by high upfront costs and somewhat unclear feasibility. For example, China, where fossil source costs for hydrogen are much lower compared to renewables, i.e., 30–40% of the cost comprises the initial upfront investments (*4*). Still, lower-cost technology is necessary to accelerate the implementation of hydrogen energetics. This includes reducing emissions that can result from fossil-fuel-operated electricity production, if electrolysis is used for hydrogen generation.

Moreover, some evaluation of hydrogen transportation, depending on the scenario, adds substantial costs (*5*). Current technologies, such as steam methane reforming (SMR), come with intrinsic CO_2 emissions, as reported by Li et al. up to 22 CO_2eq/kg H_2, with similar reports coming from the International Energy Agency (*6*). SMR currently is the most cost-effective option; however, it incurs significant taxation and social costs due to the aforementioned emissions. While the implementation of carbon capture and storage (CCS) technologies is an alternative, their installation increases hydrogen costs by up to 60% (*7*). Notably, depending on the source of electricity production, overall CO_2 emissions substantially vary. As it was shown by Kumar et al. in an investigation of hydrogen production pathways in Wyoming, USA, the addition of CCS and the use of such hydrogen is a viable option (*8*); similar conclusions were reached by Li et al. (*4*). However, in both cases, partial feasibility stems from increased social and tax costs; otherwise, CCS is a considerable expense, thereby hindering the implementation of the hydrogen economy. There is a sizeable socio-political obstacle that, as always with new technologies, involves a chicken-and-egg dilemma: infrastructure and offtake. The offtake is not being directly developed, as there is only limited production. Yet, production is not increasing to the necessary scale due to the limited offtake, which does not make it viable from an economic perspective. However, an underlying problem can be summarized in one essential term: cost. It is not just straightforward; we must remember that many components contribute to this term, including policy, availability, transportation, production, social pressure, and others.

For the sake of argument, we can focus on the generalized term 'cost.' We need to ensure low cost to decrease this term and make hydrogen more available. It is enabled when we use lower-cost raw materials or sources, such as methane, which is currently a fossil fuel but could become biogenic in the future. Let's consider fossil methane as an example; in Latvia, similarly to Lithuania, a network of natural gas pipes spans the country, simplifying transportation, as the necessary technology already exists. But mainly due to a lack of policy allowing hydrogen transportation via this network. Moreover, if our goal is to accelerate the adoption of hydrogen energetics, we need to have means of transportation. In the case of Latvia, investigations have demonstrated the feasibility of utilizing the existing infrastructure (*9*,*10*). However, for high-purity and large-scale hydrogen transportation, a new network or at least an upgrade of the existing network is required due to the impact of H_2 on current pipes (*11*). On the other hand, a natural gas infrastructure and network already exist; using methane could be a viable solution without incurring upfront costs. Let's not forget that standard SMR, or grey and blue hydrogen, still comes with social and monetary costs. There is a need to find alternative technologies that can mitigate the burden imposed by current fossil-fuel-based technologies while advancing a sustainable, implementable hydrogen economy.

Investigation of available options reveals alternative technologies, e.g., turquoise hydrogen or thermal methane decomposition. In contrast, green hydrogen is set aside due to the mentioned goals of eventual transfer, as well as the lack of power, resources, and offtake among other factors (*12*). Some require significant capital, while others require existing infrastructure. Given our existing infrastructure for grey/blue hydrogen, there is only one option for our purposes. Thus, in the transition period, we aim to substitute grey and blue hydrogen with turquoise hydrogen to lower costs and improve not only environmental gains in the adaptation of hydrogen but also the production of valuable carbon-based sensors/devices (*13*), thus opening a new supply chain option and revenue stream (*14*).

There are variations of turquoise hydrogen, depending on the heating method, reactor type, and other parameters. A promising option is to use catalysts to increase efficiency. It is known that various catalysts can be selected in multiple forms, compositions, and with different supports. We have shown a brief summary of various standalone catalysts for methane conversion rates (*15*). But catalyst on support with a large surface area, as was done by Wang et al., where Ni/Al_2O_3 impregnated with co-catalysts such as Fe, Cu, Pd, Zn, Ni, Co, or by Iliopoulou et al. with Co/Fe with Pd co-catalyst on γ-alumina support *16*–*18*). It is noteworthy that these catalysts can be used for methanol reduction as well as methane decomposition (*19*). Iliopoulou et al. noted that Ni is deactivated above 600°C, whereas Fe requires high temperatures for activation. Experimentally, they achieved a 20% conversion rate at 850 °C (*18*). All indications suggest that higher temperatures or reduced catalysts may occur before thermocatalytic decomposition, leading to the formation of various active surface species, such as Fe_3C, $FeAl_2O_4$, or others. Thus, there is a need to develop simplified, scalable methods for catalyst production and investigation.

Ni–Fe bimetallic catalysts for methane pyrolysis have been investigated due to their synergistic catalytic behavior. Nickel facilitates methane dissociation, while iron improves catalyst stability and promotes filamentous carbon formation, reducing deactivation. Several studies have demonstrated enhanced hydrogen production and carbon nanostructure growth over Ni–Fe catalysts supported on Al_2O_3 and other materials (*16*,*17*,*20*,*21*).

In this work, we investigate the influence of catalyst composition on turquoise hydrogen production at 700, 800, and 900 °C, and examine the content and yields of the by-products. A catalyst architecture consisting of Fe with Ni nanoclusters deposited on a γ-alumina support was synthesized using magnetron sputtering. While Fe–Ni catalysts are well established, the novelty of this work lies in the controlled formation of a non-alloyed Fe–Ni architecture, where discrete Ni nanoclusters are deposited on metallic Fe layers. Unlike conventional catalysts prepared via co-impregnation or based on iron oxides, the present approach enables the use of metallic Fe and control over metal distribution, avoiding uncontrolled phase formation and enabling systematic tuning of catalyst structure. In addition, the use of Ni in the form of nanoclusters allows reduced metal loading while maintaining catalytic functionality. This architecture provides a platform to investigate structure–performance relationships and catalytic activity at lower temperatures.

The aim of this study is to investigate how iron content affects hydrogen production, assuming that increased iron content increases hydrogen content proportionally. The addition of a Ni co-catalyst is expected to reduce the activation temperature for methane cracking while improving the overall catalyst stability.

Experimental setup and material synthesis

Fe catalysts embedded with Ni nanoclusters were synthesized via physical vapor deposition (PVD) using a PVD 75 system (Kurt J. Lesker Co.). A dual-magnetron sputtering system was employed, utilizing high-purity (99.99%) Fe and nickel cathodes as the respective target materials. Commercially available gamma-phase γ-Al_2O_3 powder (Testbourne) was used as the substrate for catalyst synthesis. The powder has a high purity and a surface area of 130 ± 20 m^2/g. Full deposition description is discussed in the Supplementary nformation in the Material synthesis section. Shortly, γ-Al_2O_3 was evenly distributed as a monolayer in a Petri dish. The target-to-alumina distance was 8 cm. The deposition of Fe was conducted first with varying loadings; the deposition times were set to 2 min 30 s, 5 min, and 7 min 30 s, respectively. For the synthesis of Ni nanoclusters, the current and voltage were set to lower values with a deposition time of 18 s. The Ni deposition time was optimized based on previous experimental studies to promote the formation of discrete nanoclusters.

The complete synthesis procedure was carried out in multiple steps to ensure uniform catalyst distribution. Fe was deposited onto the γ-Al_2O_3, then it was extracted, manually mixed for redistribution, and returned for a second Fe deposition cycle. Thus, homogeneous dispersion of Fe across the γ-Al_2O_3 surface was achieved. A similar two-step approach was applied for the synthesis of Ni nanoclusters by realigning the sample under the Ni target for nanocluster formation. Similarly to Fe, after the first step, the powders were removed, thoroughly mixed, and subjected to a second Ni deposition cycle.

The pyrolysis reaction was carried out in a batch reaction using an in-house-made reactor, the schematic of which is shown in the Supplementary Information (Figure S1) and previously reported in (*22*). After loading the sample, air is evacuated using a vacuum pump, then methane is introduced into the system to a pressure of 0.5 bar. The reactor is heated to the selected temperature in 120 min and maintained at that temperature for 240 min. The methane pyrolysis or catalytic decomposition of methane (CDM) experiments were carried out at selected temperatures of 700, 800, and 900 °C to investigate catalyst composition impact at lower temperature ranges.

After natural cooling, the gas sample is taken using a Restek gas bottle with Swagelok VCR connectors and fittings and analyzed with a mass spectrometer (RGA100 MS, Stanford Research Systems, USA). Each sample is examined at least 3 times to ensure repeatability. Content is estimated based on relative peak intensity ratios, assumed constant within the MS device and assigned accordingly. MS is calibrated using industrial gas mixtures and CO from Linde gas.

Catalyst investigation

The catalyst material is investigated both before and after CDM using various experimental techniques. The morphology of the catalyst surface before pyrolysis, including surface texture, was examined using scanning electron microscopy (SEM, Hitachi S-3400N, Japan). After CDM, the samples were investigated using a Helios5 UX (Thermo Fisher Scientific, USA). SEM images were analyzed using FIJI ImageJ 1.54p.

Elemental composition analysis was conducted via energy-dispersive X-ray spectroscopy (EDS, Bruker Quad 5040, Germany) for qualitative assessment of elemental distribution. The coating thickness of the deposited material was measured using a DektakXT stylus profilometer (Bruker, Germany), which was used to measure the coating thickness on a flat surface.

The catalyst's crystal structure was analyzed by X-ray diffraction (XRD; Bruker D8, Germany) at 40 kV and 40 mA in the θ–θ configuration. The key measurement parameters included Cu Kα radiation (λ = 0.15406 nm), a scan range of 20–70°, and a 0.3° fixed divergence slit. The obtained XRD patterns were analyzed using the PDF-5 + database (ICDD) as a reference. After CDM, XRD was carried out using Rigaku MiniFlex 600 (Rigaku Corporation, Japan), operating at 40 kV and 15 mA, also using Cu Kα radiation (λ = 0.15406 nm), a scan range of 20–70°, and a fixed divergence slit.

X-ray photoelectron spectroscopy (XPS, PHI 5000 Versaprobe, USA) was employed to determine the surface elemental composition and chemical states of elements. Quantitative analysis of the XPS spectra was performed using Multipak software. The spectra were recorded with a pass energy of 187.85 eV, using monochromated Al Kα radiation (1486.6 eV, 25 W beam power), a 100 µm beam size, and a 45° measurement angle.

Raman spectroscopy was performed using a TriVista CRS Confocal TR777 system (Spectroscopy & Imaging GmbH, Germany) to characterize the structural properties of the carbon materials obtained after CDM.

Processing and characterization of electrochemical test structures

The thick film pastes were prepared from the samples after pyrolysis. In these tests, a sample of Fe(200 nm)Ni was used after CDM at various temperatures (700, 800, and 900 °C). Powders were dispersed in an organic vehicle and subsequently homogenized on a three-roll mill (Exact Technologies, Oklahoma City, OK, USA). The pastes were screen-printed in 8 mm x 8 mm square-shaped patterns on an alumina substrate (96% Al_2O_3, Rubalit 708S, CeramTec) using a screen printer (P-250AVF, KEKO Equipment, Žužemberk, Slovenia). The deposits were dried at 150 °C for 15 min in air and subsequently fired at 850 °C in an argon atmosphere as described elsewhere (*13*). The electrical connections were made using a colloidal silver paste (Ted Pella Inc., Redding, California, US), which was dried at room temperature in air and subsequently covered with a water-resistant layer of nitrocellulose. The test sensor structures, prepared from powders obtained at various CDM temperatures (700, 800, and 900 °C), are denoted as S-700, S-800, and S-900, respectively.

S-700, S-800, and S-900 were characterized by cyclic voltammetry using a potentiostat/galvanostat (Multi Autolab M204, Metrohm, The Netherlands) with Nova 2.1.5 software. Measurements were performed at 25 °C in a 50 mL cell consisting of S-700, S-800, and S-900 as the working electrode (WE), an Ag/AgCl (3.0 M KCl, Metrohm) reference electrode (RE), and a platinum sheet counter electrode (CE, Metrohm).

Phosphate buffer solution (PBS) and hexacyanoferrate (II)/(III) solution (HCF) were prepared using ultrapure water (resistivity ≥18 MΩcm). PBS with pH 7 was prepared from NaH_2PO_4 (≥99.0%, Merck, Darmstadt, Germany) and Na_2HPO_4 (Na_2HPO_4, >99.0%, Merck, Darmstadt, Germany). 1 mM hexacyanoferrate (II)/(III) solution (HCF) in PBS was prepared from $K_4[Fe(CN)_6]\cdot 3H_2O$ (≥98.5%, Carlo Erba, Val-de-Reuil, France) and $K_3[Fe(CN)_6]$ (≥99% Carlo Erba, Val-de-Reuil, France). All CVs were recorded in PBS over a potential range from −0.2 V to +0.6 V, starting from an initial potential of 0.0 V in the positive direction with a step potential of 2.44 mV. Three consecutive scans were recorded at a scan rate of 100 mV/s. Then, the CVs were recorded in 1 mM HCF solution using an identical procedure.

The CVs in a model solution of pesticide imidacloprid (IMD, $C_9H_{10}ClN_5O_2$ (≥98.0%) Sigma Aldrich, USA, 0.1 mM/L) in PBS with S-700, S-800, and S-900 were recorded between −1.5 V and +0.35 V from the initial potential of −0.2 V in the positive direction at a scan rate of 100 mV s^{-1}. The CV was recorded after 3 min of accumulation under stirring conditions (*13*).

Results

SEM was employed to analyze the morphological evolution of γ-Al_2O_3 powder surfaces following magnetron sputtering deposition of Fe and Fe with Ni nanoclusters. Representative SEM micrographs are presented in Figure 1, where Figure 1(a) shows γ-Al_2O_3 powder coated with pure Fe, deposited via magnetron sputtering for 5 min (about 200 nm). Figure 1(b–d) display Al_2O_3 powders coated by Fe with Ni nanoclusters, where the Fe component corresponds to approximate thicknesses of 100 nm (2 min 30 s), 200 nm (5 min), and 300 nm (7 min 30 s), respectively, reflecting varying deposition durations.

The investigation of the crystalline structure via XRD is shown in the Supplementary Information (Figure S2). The Diffractogram patterns of Fe films with varying thicknesses (100, 200, and 300 nm), containing Ni nanoclusters, were deposited on industrial γ-Al_2O_3 powder. The majority of γ-Al_2O_3 is present with minor θ-Al_2O_3 peaks, most likely coming from fluctuations during synthesis. Visible Fe peaks are present as expected at 45° and 65°, but only in the 300 nm sample; other sample peaks overlap with γ-Al_2O_3. Because the Ni was synthesized as nanoclusters, its amount was too small, and its diffraction signals were overwhelmed by the substrate's strong reflections and the similar positions of Fe and Ni peaks. Further analysis was conducted to address these limitations and obtain more precise phase information, utilizing XPS and EDS, as illustrated in the Supplementary Information (Figures S3 and S4, respectively).

During catalyst development and deposition on the support, gamma alumina and various Fe sputtering times were selected. Table 1 shows the sample surface content investigated by XPS. The composition of the catalyst surface (top ~10 nm) is illustrated in the Supplementary Information Figure S3, where full XPS spectra shown in S3(a). The elemental composition results indicate that oxygen and aluminum are the two most abundant elements, with concentrations of approximately 59 at. % and 26 at. %, respectively.

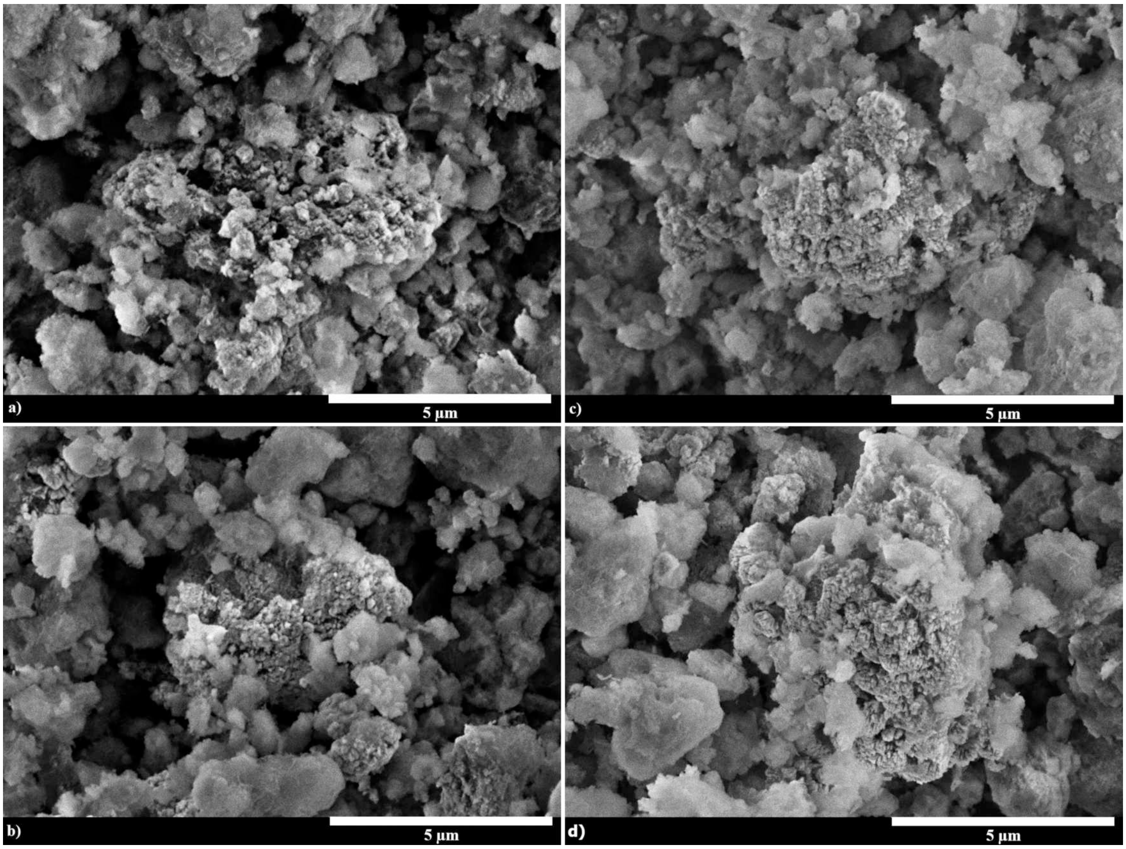

Figure 1. SEM images of γ-Al_2O_3 powders after (a) Fe and (b)–(d) Fe-Ni vapor deposition at varying iron sputtering times.

Table 1. Chemical concentration of the catalyst top-layer.

	Chemical concentration, at. %				
Sample	O	Al	C	Fe	Ni
Fe 200nm	59.8	27.6	7.1	5.5	–
Fe(100 nm)Ni	58.2	26.3	9.8	5.2	0.5
Fe(200 nm)Ni	58.5	25	10.3	5.8	0.4
Fe(300 nm)Ni	60.3	26.1	6.5	6.6	0.5

Much of the detected oxygen is attributed to the γ-Al_2O_3 support, which is composed of pure alumina. Oxygen peak is shown in Figure S3(b), with corresponding Fe2p in S3(c) and (d).

Regarding the active catalyst components, the Fe concentration varied between 5.2 at. % and 6.6 at. %, depending on the deposition time. In contrast, the Ni content remained relatively stable across all samples, averaging approximately 0.5 at. %, consistent with the short deposition duration used for nanocluster formation. These results reflect the catalyst synthesis parameters, as foreseen: first, a pure Fe catalyst, then a Fe catalyst with different concentrations, maintaining a stable amount of Ni nanoclusters. Notably, the carbon (C) concentration exhibited some variability, ranging from 6.5 at. % to 10.3 at. %, without displaying any clear correlation with synthesis parameters or sample conditions. Given that the sample synthesis procedure was conducted under identical conditions, it is presumed that environmental factors, such as ambient temperature and humidity, may have influenced the adsorption of carbon-based contaminants on the catalyst surface. Following synthesis, the catalysts were transferred to a storage vessel and kept under ambient conditions for three days prior to XPS analysis. This storage and measurement protocol was uniformly applied across all samples. Notably, extended storage beyond this period did not result in an increased carbon signal, suggesting that the initial level of carbon contamination remained stable and did not further affect the catalyst surface.

Samples show Fe^0 and oxidized Fe^{3+}, corresponding to Fe_2O_3, with a 1:7 ratio, indicating that the samples' surfaces are oxidized. Compared to XRD results show no oxide peaks, which also indicate the low amount/volume of Fe_2O_3 on the surface, oxidation is observed after synthesis.

Elemental maps of powders are shown in Figure 2. These maps confirm the successful deposition and spatial distribution of metallic layers across the surfaces of γ-Al_2O_3 particles. An isolated Fe elemental map is shown in the Supplementary Information Figure S4(a), with O and Al inclusion in (b). It shows a homogeneous distribution of iron on the particle surfaces, with no signs of clustering or surface inhomogeneity. The corresponding Fe–Al–O composite map shows Fe layer thickness increase from 100 nm to 300 nm with longer sputtering durations, respectively, in Figure 2(a) to (c). It shows distinct and overlapping signals of Fe, Ni, Al, and O, indicating that the iron layer is uniformly deposited over the γ-Al_2O_3 substrate without fully encapsulating it. In Figure 4S individual Fe and Ni element maps for samples Fe(100 nm)Ni, Fe(200 nm)Ni, and Fe(300 nm)Ni, respectively, are shown in (c, e, and g); while full maps for these samples are shown in Figure S4(d, f and h). In all cases, Fe and Ni signals are clearly co-localized, verifying the successful deposition of both elements. Compared to Fe, Ni appears more discontinuously distributed, likely forming discrete nanoscale clusters due to its significantly shorter deposition time. This granular appearance aligns with Ni's intended role as a nanoparticle-forming additive rather than a continuous film-forming species. The composite Fe–Ni–Al–O maps reveal consistent overlap among all elemental signals. This confirms that the

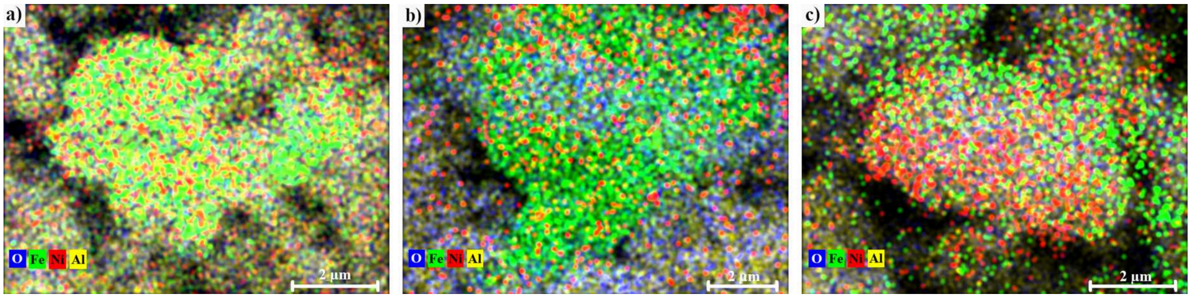

Figure 2. EDS elemental map of γ-Al_2O_3 powders after magnetron sputtering with Fe and Ni: (a) sample Fe(100 nm)Ni, (b) Fe(200 nm)Ni, (c) Fe(300 nm)Ni.

metallic coatings adhere well to the γ-Al_2O_3 surface and remain localized at the particle interface. Increasing the Fe sputtering time results in a progressive enhancement of the Fe signal intensity, indicating an increase in coating thickness. However, no significant lateral redistribution or structural disruption is observed across samples, suggesting that the deposition process maintains compositional and morphological uniformity.

Methane pyrolysis or catalytic methane decomposition

Following the CDM reaction, two primary aspects were analyzed: (i) the composition of the evolved gases and (ii) the morphology and carbon composition deposited on the catalyst surface. The gas content obtained at different CDM temperatures is shown in Figure 3. The detailed composition of the samples and the presence of other gases are shown in the Supplementary Information Figures S4 and S5, respectively. Although literature reports varying efficiencies and temperature dependencies, conventional pyrolysis typically indicates that increasing the reaction temperature enhances hydrogen production.

At the same time, it has been observed that increasing the pressure of the reaction vessel shifts the conversion rate down, e.g., to reach a 50% conversion rate at 1 bar vs 10 bar, it is necessary to increase the temperature from 500°C to 750°C, as shown by Leal Perez et al. (*23*) based on Serban et al. data (*24*). As in this case, the reactor is at 1–1.5 bar pressure we should expect around 50% at 550 °C and up to 95% at 850°C (*25*). It is noteworthy that introducing a catalyst substantially shifts production, temperatures, and heating methods. For example, in the range of 600–800°C, using microwave-assisted pyrolysis yielded from 42 to 78% at 600°C for Fe on activated carbon and above 90% with FeNi catalysts on activated carbon, while also reaching a high 90% using conventional heating (*21*). Even though the main focus of methane pyrolysis is the turquoise hydrogen, in thermochemical cracking with catalysts variations in C + products can occur. Such as C_2H_6, C_6H_6, and others(*26–28*).

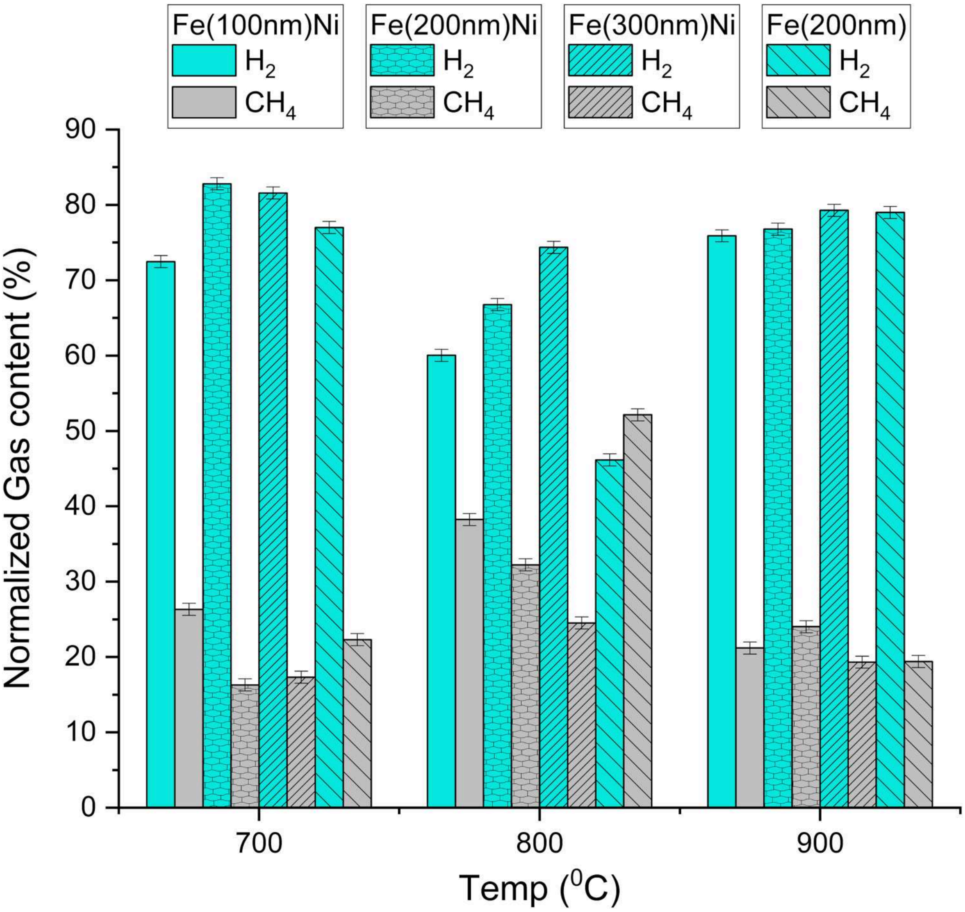

Figure 3. Gas analysis results. CH_4 and H_2 content in samples after CDM at 700, 800, and 900 °C reaction temperatures.

In this work, the catalyst has substantial space for methane to access and travel around the reactor volume; thus, we can assume that the catalyst is fully exposed to methane. The results of CH_4 and H_2 content are shown in Figure 3, where an increasing amount of Fe corresponds to a rising hydrogen content and CH_4 conversion rate. An increasing amount of Fe leads to an increase in H_2 from 73% to 83% and 82%, respectively, while Ni-free samples show 77%. At 800 °C, the change is more substantial, from 60% to 75% vs 40% for the Ni-free sample. On the other hand, at 900 °C, the Fe(200 nm) sample shows the highest hydrogen content of 90%, while Ni-containing samples are below 80%. CH_4 conversion rates are more comparable; moreover, we have a comparable amount of hydrogen at 700 °C for the Fe(300 nm)Ni sample to 900 °C, which indicates higher process efficiency, with conversion swings from 95% to 93%, while intermediate amount of Fe, the sample Fe(200 nm)Ni, has a change from 93% to 94% %, respectively. The lowest conversion rate comes has a lower CH_4 content compared to the Fe(100 nm)Ni sample, while the Ni-free sample shows a lower CH_4 content compared to Fe(100 nm)Ni, which shows conversion rates from 92% to 89%. The hydrogen content at 700 °C is comparable to or even exceed those obtained at higher temperatures, indicating a possible temperature-dependent shift in reaction pathways and carbon deposition behavior. This shows that the use of as prepared catalyst without the necessary activation or reduction of Fe can be mitigated by addition of Ni nanoclusters, that is the reduction of surface iron oxide to open catalytic sites. This behavior may be attributed to the specific catalyst architecture employed in this work, where discrete Ni nanoclusters are distributed on Fe layers rather than forming conventional alloyed systems. Such a configuration can enhance methane activation at Ni sites while maintaining structural stability through the Fe phase. The clear distinction or reason for lower yields at 800 °C is yet to be found.

To benchmark the present catalyst, the most comparable literature is direct Fe-Ni methane decomposition on alumina-based systems; summary is shown in Table 2 and CH_4 conversion rates in Table S1. Although exact comparison remains difficult as our experiments were conducted in a sealed fixed-bed reactor at 0.5 bar CH_4 with a 120 min heat-up and 240 min isothermal hold, whereas most literature studies employ continuous-flow reactors near atmospheric pressure. The closest direct comparison is Ni-Fe/Al_2O_3 reported by Bayat et al., for which maximum H_2 yields of 41%, 58%, and 68% were reported at 700°C, 800°C, and 900°C, respectively. In the present work, the Fe thin film/Ni nanocluster/gamma-Al_2O_3 catalyst provided ~82%, ~75%, and ~80% at the same temperatures. This indicates that the present catalyst reaches a highly effective state already at 700 °C, where its H_2 yield exceeds the closest direct Fe-Ni/Al_2O_3 benchmark and approaches that of literature system's 900 °C maximum. Since the H_2 production does not improve further at 900 °C and is lower at 800 °C, the data suggest that the present catalyst architecture achieves a favorable balance between methane activation and catalyst-state evolution already at the lower temperature, which is beneficial from the standpoint of energy demand and thermal load. This interpretation is also consistent with the broader literature context summarized in our previous article by Sika et al. (*15*), where alumina-supported Fe catalysts are typically reported in the ~60-62% H_2-yield range.

Table 2. Comparative result table.

Study	Catalyst / support	Reactor mode	Key conditions	Reported H_2 metric
This work	Magnetron-sputtered Fe thin film + Ni nanoclusters / gamma-Al_2O_3	Sealed fixed bed	0.5 bar CH_4; 700, 800, 900 °C	~82% at 700 °C; ~75% at 800 °C; ~80% at 900 °C
Bayat et al. (*29*)	Ni-Fe/Al_2O_3	Methane decomposition alumina-supported direct Fe-Ni benchmark	700, 800, 900 °C	41% at 700 °C; 58% at 800 °C; 68% max at 900 °C; 47% at 900 °C after 360 min
Wang et al. (*30*)	Hydrotalcite-derived Ni-Fe/Al_2O_3 alloy catalysts	Methane decomposition direct Fe-Ni alloy benchmark	600 °C; Ni-Fe-Al hydrotalcite precursor; alloy catalyst after calcination/reduction	Study emphasizes improved catalyst life, sintering resistance, and carbon yield for composition-uniform Ni-Fe alloy catalysts
A.S.Al-Fatesh et al. (*31*)	Fe/Al_2O_3, Fe-Ni bimetallic alloy/Al_2O_3	Fixed-bed flow microreactor	Atmospheric pressure, CH_4/N_2 = 1.5/1; 700 °C	≈58–64% (estimated from plotted H_2-yield curve)
Sika et al. (*15*)	Fe/Al_2O_3; Ni/Al_2O_3	Fixed-bed methane decomposition over alumina-supported Fe	700 °C	eview summarizes alumina-supported Fe systems as typically giving about 60–62% H_2 yield

All samples provide similar CO_2 results for all tested temperatures. Similarly, it can be observed that at 800°C, all yields are lower for all samples. The gas analysis showed that the gas sample composition varies with both the sample and the temperature. Notably, some residual components are also visible, including water, nitrogen, CO, and CO_2, with varying amounts, as shown in the Supplementary Information (Figure S5). Although we may aim for 100% conversion, there are alternative use cases.

To some extent, the blend of CH_4 and H_2 (hythane) can be directly used in specific applications, depending on the ratio and various properties of these mixtures, as summarized by Hora et al. (*11*). Typically, hythane is mixed externally, necessitating specialized mixing stations. However, if we replace it with on-site catalytic synthesis, it could lower overall costs by eliminating H_2 production off-site, mixing costs, and overall emissions. Pyrolysis in various combinations, i.e., molten catalysts or electrified pyrolysis (*32*,*33*), have been evaluated as more efficient and at a lower cost. On the other hand, the hythane has been shown in the automotive industry with lower CO_2 emissions and no modifications (*34*–*36*), though, as summarized by Anand et al. pyrolysis is explicitly not widely considered for hythane production (*37*). Using hythane could lower costs and accelerate the transition to hydrogen energetics by leveraging existing infrastructure. To the best of our knowledge, based on cost calculations, the assumed operational temperature is around 1000 °C. This compares to the catalyst presented in this work, which shows efficiency at 700 °C exceeding that at higher temperatures. This suggests the potential feasibility of these catalysts and, consequently, the suitability of the synthesis technology.

After pyrolysis analysis

Carbon deposition

As previously discussed, a crucial component of catalytic methane decomposition and lower CO_2 emissions is the deposited solid carbon. It is projected as an additional revenue stream and will play a substantial role in the final cost of hydrogen, depending on the quality and quantity of such carbon material. In this work, the estimated hydrogen content is shown in Figure 3, and the carbon yield evaluation is presented in Figure 4, calculated following Al-Fatesh et al. (*38*). Comparing samples based on Fe content reveals a pattern of C deposition increasing with Fe content. In contrast, the sample without Ni exhibits lower overall C deposition,

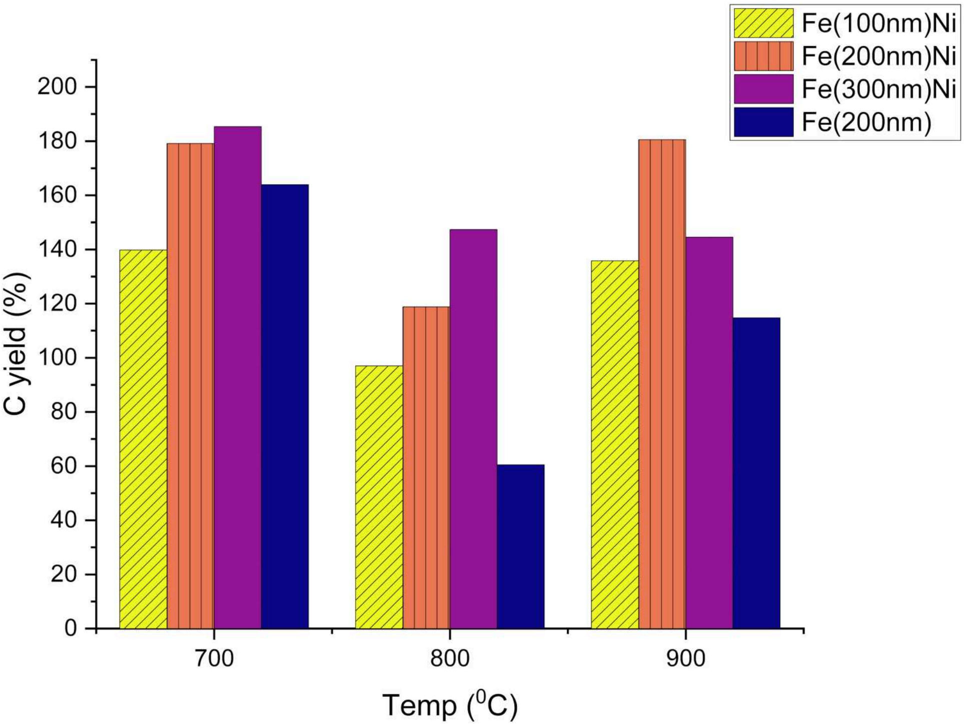

Figure 4. Carbon yields after the reaction. Lower temperatures provide overall larger or comparable yields to the highest tested temperature, indicating higher overall efficiency.

except at 700 °C, compared to the sample with a lower Fe amount. The addition of a co-catalyst promotes carbon yields.

The composition and amount of carbon produced during CDM will play a crucial role in the technology's feasibility. While the social costs associated with lower CO_2 emissions are already lower than those of conventional SMR, generating high-value carbon products can further improve economic viability. For example, carbon can be used in batteries (*39*), catalysts for methane thermal cracking (*40*), or for hydrogen storage (*41*). The market value varies widely: carbon nanotubes are sold at retail prices ranging from \$60 to \$1,400 per gram (Millipore Sigma), whereas bulk suppliers like Alibaba offer around \$180 per kilogram. Orozco et al. summarized prices from 1 to 100 USD per gram, depending on the material type (*42*). Therefore, it is vital to identify the type of carbon deposited on the catalyst. Several mechanisms have been proposed for the growth of carbon nanotubes or fibers during CDM. For example, using Ni-based catalysts, deposited carbon can encapsulate small particles and push larger particles upward, leading to fiber or tube growth (*43*). SEM and EDS analysis confirm the expected catalyst composition, consisting of a $\gamma - Al_2O_3$ support and Fe/Ni catalysts. After CDM, various carbon deposits are observed, including nanowires and nanofibers (CNFs), as well as larger agglomerates on the catalyst surface.

In this work, SEM analysis of samples after pyrolysis reveals clear carbon fibers on all samples. Similar morphologies and composition were reported by Iliopoulou et al., where carbon fibers grow comparably (*18*). Carbon can form various geometries and lengths depending on the catalyst, but the reaction conditions play a significant role. Song et al. summarized these variations of carbon forms, including CNFs, carbon nanotubes, carbon nano-onions, and graphitic structures (*26*). Additionally, Hantoko et al. noted that carbon nanotubes could grow depending on the catalyst size, type, and material (*43*). The type of carbon growth also depends on the catalyst's crystalline phase, including changes resulting from catalyst surface reduction, which may lead to slight variations depending on the catalyst composition. In this work, Fe_2O_3 and Ni are present, and the reduction of iron oxide occurs as the reaction progresses; thus, a possible rearrangement of the surface may occur. As shown in Figure 5, with additional details provided in Supplementary Information Figures S6 and S7. Figure 5(a) and (b), as well as S6(a) and S7(a) show Fe(100 nm)Ni SEM micrographs, respectively, at 700°C, 800°C and 900°C, where long CNFs on and around catalyst are visible. Similarly, Figure 5(c) and (d) as well as S6(b) and S7(b) depict sample Fe(200 nm)Ni SEM micrographs at the same temperatures at various magnifications. Figure 5(e) and (f), as well as S6(c) and (c) depict Fe(300 nm)Ni at set temperatures and magnifications. SEM reveals that carbon growth shows slight variations depending on Fe content and reaction temperature. In most cases, CNFs are observed, with varying lengths, diameters, and degree of agglomeration, including substantial twisting and nets. Similar CNFs have been reported in the literature (*16*,*17*).

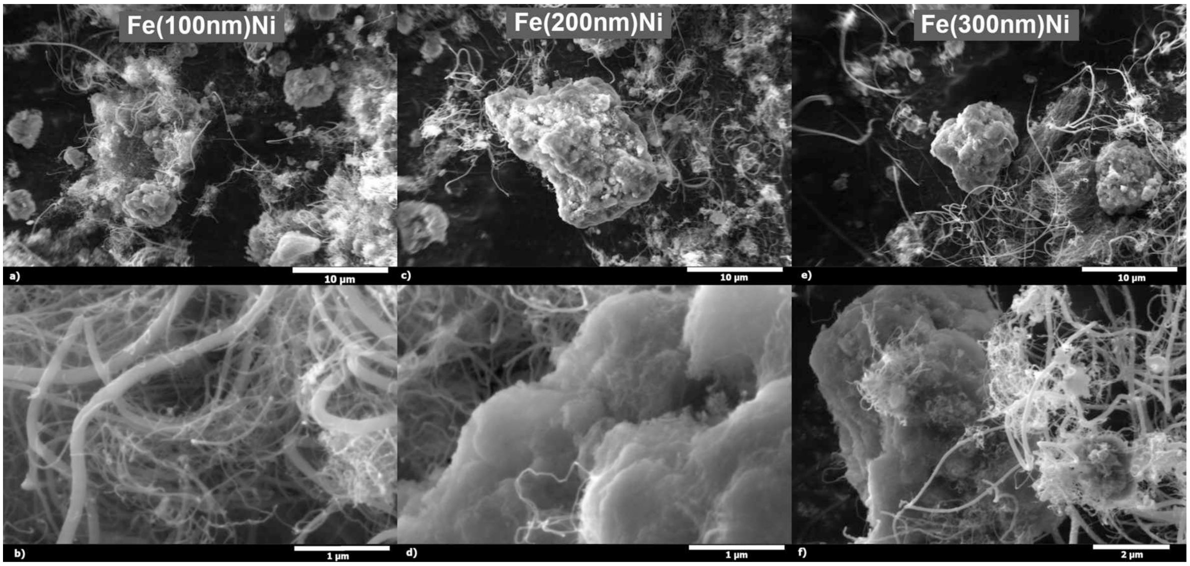

Figure 5. SEM micrographs of samples after reaction at 700 °C. Carbon nanofibers are present in all samples with slightly varying diameters.

Comparison of CNF geometries (Figures S6 and S7) reveal differences in fiber diameter, which depend on the pyrolysis temperature. At higher temperatures, diameter changes are negligible, with an average of approximately 50 ± 8 nm. On the other hand, at the lowest tested temperature, substantially larger-diameter CNFs were identified for Fe(100 nm)Ni an average diameter of about 160 nm. In contrast, the Fe(200 nm)Ni and Fe(300 nm)Ni samples had similar diameters of roughly 50 nm. A summary of the results is shown in the Supplementary Information Figure S8, and corresponds to the proposed CNF growth mechanism on the metallic nanoparticles, as discussed previously (*43*).

Analysis of crystalline structure

As shown in Figures S2 and S3, the initial composition of the catalysts included gamma alumina, nickel, iron, and iron oxide. As discussed previously, partial reduction of iron oxide occurs during the pyrolysis process. After the pyrolysis reaction, substantial deposition of carbon is observed, along with possible alumina and catalyst phases, as shown in Figure 6 for Fe(100 nm)Ni and in the Supplementary Information, Figures S9 and S10, for Fe(200 nm)Ni and Fe(300 nm)Ni, respectively.

The deposited carbon shows strong graphitic and CNT peaks. Similar pyrolytic carbon structures have been reported in the literature for fixed-bed, fluidized-bed, and molten salt pyrolysis systems (*44*). Investigation of Fe, Ni, and Co catalysts and grown carbon structures revealed significantly more oriented carbon growth on the Ni catalyst, indicating the presence of Fe and Ni, as well as C peaks in the XRD data (*45*). The results in this work are consistent with those of Awadallah et al., who identified carbon growth and corresponding XRD patterns. Notably, variations in catalyst composition can significantly influence results, as demonstrated by Torres et al. in their study of reduced Ni catalysts supported on various materials. They reported diffraction peaks corresponding to Ni (111), (200), and (220) planes at 2θ values equal to 44.5°, 51.6°, and 76.4°, respectively, in agreement with literature data (*46*). After pyrolysis, NiO phases were identified with (111), (200), (220), (311), and (222) planes at 2θ values of 37.2°, 43.3°, 62.7°, and 79.3°. In this study, the Ni content is relatively small and does not appear in the initial XRD patterns before pyrolysis. Moreover, Ni and NiO peaks overlap with C, Fe, and alumina peaks; therefore, the reflections are attributed to the predominant phases, while the presence of minor Ni or NiO peaks cannot be excluded.

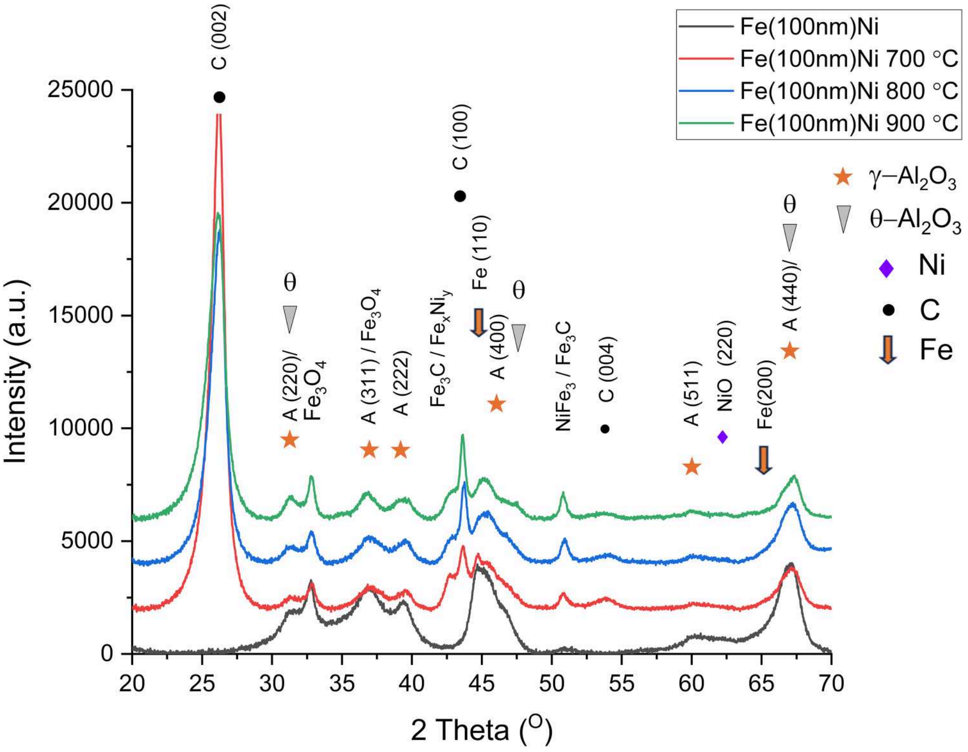

Figure 6. XRD diffractogram of sample Fe(100 nm)Ni before and after pyrolysis at 700°C, 800°C, and 900°C.

Additionally, the observed peak positions are consistent with previously reported data (16,17,47,48), confirming that the crystalline structure has changed after the reaction. Although the samples were handled in an ambient atmosphere after reaction, no visible reoxidation to Fe_2O_3 was detected, indicating that the reduced Fe had formed other compounds, such as Fe_3C, $NiFe_3$, and Fe_3O_4, in addition to carbon deposition.

From these considerations Ni appears to play a dual role in the Fe–Ni/γ-Al_2O_3 catalyst: first, by facilitating reduction/activation of Fe-containing oxide species, and second, by favoring the formation of mixed metallic or carburized active phases during methane pyrolysis. Literature on alumina-supported methane decomposition catalysts shows that Ni promotion can enhance Fe reducibility, while reduced Ni–Fe/Al_2O_3 systems can contain Ni–Fe alloy phases. One of existing reaction pathways suggests dissociation of chemisorbed CH_4 (49) followed by the diffusion of carbon either through metallic catalyst or over its surface (50,51). Then it is noted that diffusion rate, and thus, the activity of methane reduction, partially depends on this carbon diffusion, which is limited to concentration gradient. Since Fe_3C formation under methane has also been reported for alumina-supported Fe catalysts (17), the XRD features observed here are reasonably assigned to a combination of reduced Fe, possible Fe_3C, and possible Ni–Fe alloy phases. It has been noted that Fe_3C stability decreases with temperature. If we look for relative changes in XRD peak ratios to estimate the phase composition, it could indicate decrease of Fe_3C and increase in alloy content here we can see intensity changes of said reflections following this trend as shown in Figures S11–S13. In combination with carbon deposition and yields, this would point towards Ni combination with Fe lowers activation energy, nevertheless, due to peak overlap, we avoid overinterpreting the diffractograms and describe these assignments as XRD-consistent rather than definitive.

These phase transitions may substantially influence the reusability of the investigated catalysts and should be taken into consideration in future studies.

Raman spectroscopy

Raman spectroscopy spectra for the tested samples are shown in Figure 7. As observed in the SEM analysis, CNFs exhibit similar morphologies, with slight deviations in size depending on temperature. Raman spectroscopy was used to further investigate the structural characteristics of carbon materials.

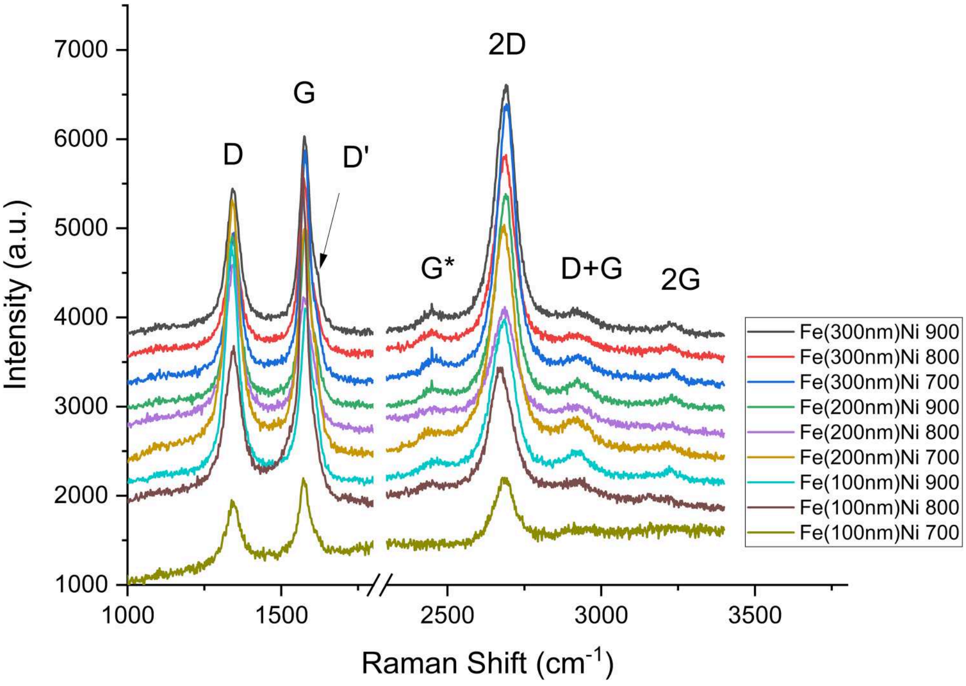

Figure 7. Raman data for all samples. Samples exhibit consistent C vibrational modes, with D, G, and 2D modes also present. Some samples indicate D′ presence.

In carbon-based structures, three main vibrational modes, designated as D, G, and 2D bands, typically appear at around 1360, 1560, and 2700 cm^{-1}, respectively (*52*). These are typical of all sp^2-bonded carbon materials, including graphite, graphene, carbon nanotubes, and CNFs, but their exact shape, intensity, and position differ depending on the material's structure (*53*). For example, Patzschke et al. found distinct D and G bands at around 1350 and 1585 cm^{-1} of carbon materials derived from methane pyrolysis (*44*). It is noteworthy that a weak G* band appears after CDM at approximately 2450 cm^{-1}, which is typically associated with second-order Raman scattering in disordered graphitic structures. A similar feature has been observed in other carbon materials by Shimada et al. (*54*).

In this work, the Raman spectra exhibit very similar forms, consistent with the typical features of CNFs, which feature the three aforementioned modes. As observed in the SEM images, the CNFs are highly bent and twisted, which can induce a shift in the G band position (*53*). The presence of both D and 2D (also referred to as G′) bands indicate structural disorder and defects within the deposited carbon (*55*). It is noteworthy that the amount of disorder is dependent on the catalyst amount and type.

Similar results have been reported previously, i.e., Patzschke et al. investigated the I_D/I_G and G-band position in carbon materials obtained from methane pyrolysis (*44*). Comparable results were obtained in this work, I_D/I_G ratios are shown in the Supplementary Information Figure S14(a), while the G band shift in Figure S14(b). A shift of the G band towards 1580 cm^{-1} indicates the presence of amorphous carbon. The I_D/I_G increase corresponds to a higher degree of disorder and amorphization within the carbon structure (*55*). Changes in this ratio can be interpreted in terms of structural defects and the degree of graphitization (*44*,*56*). This result aligns with SEM and XRD observations, which indicate partial crystallinity and ordered growth of CNFs. The temperature-dependent increase in the I_D/I_G ratio suggests that kinetic effects influence the extent of carbon disorder. Additional elemental analysis, as shown in Figures S15 to S17, respectively, for samples Fe(100 nm)Ni to Fe(300 nm)Ni, confirms XRD, SEM, and Raman data, with increased temperature C deposition increases by covering active sites.

Electrochemical characterization of test sensor structures

The CVs of S-700, S-800, and S-900 measured in PBS and HCF are shown in Figure 8(a). The capacitive current of the samples increased with increasing pyrolysis temperature, as evidenced by the CV measurements in PBS (Figure 8, dashed line). In HCF, the reduction and oxidation current peaks at approximately 0.05 and 0.35 V, respectively, were well defined for S-700 and S-800, while broad, indistinct peaks were observed for S-900. For all samples, the absolute values of i_{pa} and i_{pc} increased with increasing CDM temperature, while the i_{pa}/i_{pc} ratio remained relatively constant at approximately one for all samples. The CVs of S-700 and S-800 showed similar peak-to-peak separation (ΔE_p), 232 and 237 mV, respectively. This separation was significantly larger for S-900, 474 mV. The half-wave potential ($E_{1/2}$) increases with increasing CDM reaction temperature (Table S2). The results suggest that the S-700 and

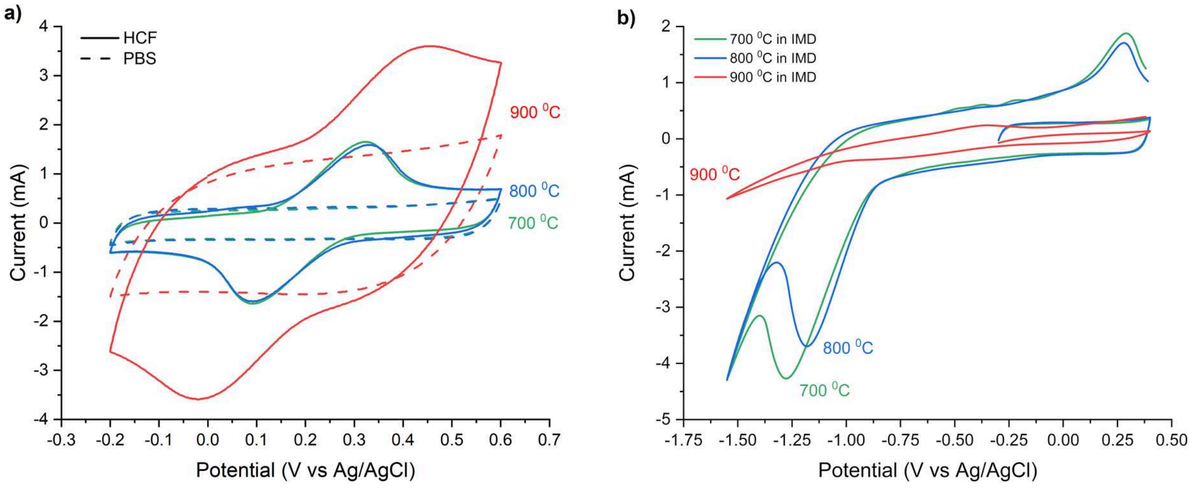

Figure 8. Cyclic voltammograms of S-700, S-800, and S-900 recorded in (a) 0.1 M PBS (dashed lines) and 1 mM HCF in 0.1 M PBS (solid lines); (b) in PBS (dashed lines) and IMD (solid lines).

S-800 performed better than the S-900 in HCF. Based on these results, we tested the response of S-700, S-800, and S-900 in a solution of the model neonicotinoid pesticide imidacloprid. A cathodic peak I_{pc} is characteristic of the irreversible reduction of the -NO_2 to -NHOH functional group (*57*). As it is clearly visible in Figure 8(b) for S-700 and S-800 at of −1.276 V and −1.166 V, both vs. Ag/AgCl, respectively, while the response of S-900 is negligible. The trends in the current response of the samples in IMD are similar to those in HCF.

Our measurements illustrate that the thick film structures prepared from carbon powders originating from the pyrolysis reaction at 700°C and 800°C are electrochemically active in model solutions of HCF as well as in a model solution of the pesticide imidacloprid. These powders, a byproduct of hydrogen production, can be used to process miniature electrochemical sensors for the detection of hazardous substances with redox-active nitro functional groups, such as neonicotinoid pesticides.

Conclusions

This work investigates a novel catalyst for the catalytic pyrolysis of methane. Using commercial gamma alumina as support, Fe was sputtered at various intensities, followed by the deposition of Ni nanoclusters. These materials were characterized and tested for CDM at different temperatures to lower the reaction temperature while maintaining hydrogen conversion efficiency. The Ni nanoclusters were found to promote the CDM reaction and carbon fiber growth, while the amount of Fe influenced the overall CDM efficiency. This work demonstrates that the sputtered Ni nanoclusters on Fe enabled a decrease in reaction temperature, achieving comparable hydrogen production of 82% at 700 °C and 80% at 900 °C for the highest Fe content. When comparing the influence of the Ni co-catalyst, overall carbon yields ranged from 56% at 800°C to 114% at 900°C without Ni, whereas the addition of Ni increased the yield to 118% and 180% at the same temperatures.

These results demonstrate that using a scalable method, such as magnetron sputtering, provides a viable option for producing catalytic systems with increased efficiency. Furthermore, the use of co-catalyst systems can reduce the required reaction temperature while delivering hydrogen yields comparable to or higher than those obtained with Ni and Fe alone, confirming the synergistic effect of Ni and Fe in CDM for producing turquoise hydrogen. In addition, this work presents an investigation into the structural evaluation of the catalysts and the resulting carbon deposition, thereby contributing to the knowledge base on methane pyrolysis and the forms and structures of deposited carbon. Variations in catalyst composition and CDM temperature led to predictable changes in the type and nature of carbon deposits. Further utilization of spent catalyst and carbon plays a crucial role in achieving a circular, sustainable future. As shown in this work, one application is the production of pesticide sensors, not only extending the material lifecycle but also adding further crucial value.

Acknowledgements

The authors express their gratitude to Barbara Repič (JSI) and Anna Urh (JSI), as well as Laimonis Jekabsons (ISSP UL), for their technical assistance.

Author contributions

CRediT: **Ainars Knoks:** Conceptualization, Formal analysis, Funding acquisition, Investigation, Methodology, Writing – original draft, Writing – review & editing; **Liga Grinberga:** Formal analysis, Funding acquisition, Project administration, Supervision; **Raitis K. Sika:** Investigation, Writing – review & editing; **Liga Ignatane:** Investigation, Visualization; **Marius Urbonavicius:** Data curation, Funding acquisition, Investigation, Resources; **Simona Tuckute:** Formal analysis, Investigation, Visualization, Writing – review & editing; **Janis Kleperis:** Funding acquisition, Investigation, Resources, Supervision; **Izabela Curkovic:** Investigation, Visualization; **Danjela Kuscer:** Funding acquisition, Investigation, Project administration, Supervision, Writing – review & editing; **Sarunas Varnagiris:** Conceptualization, Formal analysis, Funding acquisition, Project administration, Supervision, Validation, Writing – review & editing.

Disclosure statement

No potential conflict of interest was reported by the author(s).

Funding

This work was supported by M-ERA.NET program in cooperation with the Latvian Scientific Council under grant number No. ES RTD/2023/15; the Research Council of Lithuania under grant number No. S-M-ERANET-23-1/PFS_INNOH_23-1; and by the Slovenian Research and Innovation Agency through the research projects P2−0105, and Ministry of Higher Education, Science and Innovation of Republic Slovenia grant number C3360−23−252004.

Data availability statement

The authors confirm that the data supporting the findings of this study are available within the article and its supplementary materials and can be obtained from the corresponding author upon reasonable request.

References

[1] European Commission. European Clean Hydrogen Alliance - European Commission. European Commission. https://single-market-economy.ec.europa.eu/industry/industrial-alliances/european-clean-hydrogen-alliance_en (accessed May 28, 2025).

[2] European Commission. https://h2v.eu/ (accessed May 28, 2025).

[3] Commission, E. Clean Hydrogen Partnership. https://www.clean-hydrogen.europa.eu/index_en (accessed May 28, 2025).

[4] Li, Y.; Hao, J.s.; Zhou, Y. Economic analysis of different hydrogen production routes under a CO2 pricing mechanism – A levelized cost of hydrogen based study. *Int. J. Hydrogen Energy*. **2025,** *128*, 47–67. DOI: 10.1016/j.ijhydene.2025.04.185.

[5] Demir, M.E.; Dincer, I. Cost assessment and evaluation of various hydrogen delivery scenarios. *Int. J. Hydrogen Energy*. **2018,** *43* (22), 10420–10430. DOI: 10.1016/j.ijhydene.2017.08.002.

[6] International Energy Agency. *Global Hydrogen Review 2023*. **2024**, 1–321. DOI: 10.1787/cb2635f6-en.

[7] Li, J.; et al. The carbon footprint and cost of coal-based hydrogen production with and without carbon capture and storage technology in China. *J. Clean. Prod*. **2022,** *362*, 132514. DOI: 10.1016/j.jclepro.2022.132514.

[8] Kumar, D.; Zhang, C.; Holubnyak, E.; Demirkesen, S. Integrated assessment of levelized costs of hydrogen production: Evaluating renewable and fossil pathways with emission costs and tax incentives. *Int. J. Hydrogen Energy*. **2024,** *95*, 389–401. DOI: 10.1016/j.ijhydene.2024.11.261.

[9] Kleperis, J.; Boss, D.; Mezulis, A.; Zemite, L.; Lesnicenoks, P.; Knoks, A.; Dimanta, I. Analysis of the Role of the Latvian Natural Gas Network for the use of Future Energy Systems: Hydrogen from Res. *Latv. J. Phys. Tech. Sci*. **2021,** *58* (3), 214–226. DOI: 10.2478/lpts-2021-0027.

[10] Kleperis, J.; Zemīte, L.; Lesničenoks, P.; Dimanta, I.; Knoks, A. Hydrogen as Energy Carrier in Latvian Gas Infrastructure. 35th International Scientific Conference of Institute of Solid State physics, University of Latvia, Riga, Latvia **2019**.

[11] Hora, C.; Dan, F. C.; Secui, D. C.; Hora, H. N. Systematic Literature Review on Pipeline Transport Losses of Hydrogen, Methane, and Their Mixture, Hythane. *Energies*. **2024,** *17* (18) DOI:10.3390/en17184709.

[12] Mural, R.; Floyd, M.; Berns, S.; Takahashi, A. *Belfer Center for Science and International Affairs HARVARD Kennedy School*. 2025. https://www.belfercenter.org/research-analysis/stimulating-clean-hydrogen-demand-current-landscape#footnote-26 (accessed December 10, 2025).

[13] Repič, B.; Marolt, G.; Kuscer, D. Carbon-based thick films for electrochemical detection of neonicotinoid insecticides. *J. Electroanal. Chem*. **2025,** *984*, 119054. DOI: 10.1016/j.jelechem.2025.119054.

[14] Benani, N.; Yang, P.; Miwornunyuie, N.; Wang, T.; Wu, D.; Wang, F.; Chen, J.lin; Lv, S.; Mao, G. Bridging blue carbon and carbon markets: An interdisciplinary analysis of research and technology for climate mitigation. *Ocean Coast. Manag*. **2025,** *269*, 107808. DOI: 10.1016/J.OCECOAMAN.2025.107808.

[15] Sika, R.K.; Knoks, A.; Grinberga, L. A Short Review of Turquoise Hydrogen Production via Methane Pyrolysis Over Catalytic Systems. *J. Phys. Tech. Sci*. **2026,** *63* (1), 3–15. DOI: 10.2478/lpts-2026-0001.

[16] Pudukudy, M.; Yaakob, Z. Methane decomposition over Ni, Co and Fe based monometallic catalysts supported on sol gel derived SiO2 microflakes. *Chem. Eng. J*. **2015,** *262*, 1009–1021. DOI: 10.1016/j.cej.2014.10.077.

[17] Abdel-Fattah, E.; Alotaibi, M. A.; Alharthi, A. I. Thermo-catalytic methane decomposition over unsupported Fe–Al and Co–Al catalysts for hydrogen and carbon nanostructures production. *Int. J. Hydrogen Energy*. **2024,** *64*, 685–694. DOI: 10.1016/j.ijhydene.2024.03.306.

[18] Pachatouridou, E.; Zeza, E.; Lappas, A.; Iliopoulou, E. Study of Co/γ-Al2O3 and Fe/γ-Al2O3 materials for catalytic methane pyrolysis to CO2-free hydrogen. *Int. J. Hydrogen Energy*. **2025,** *101*, 785–796. DOI: 10.1016/j.ijhydene.2024.12.383.

[19] Hu, B.; Shu, R.; Tian, Z.; Wang, C.; Chen, Y.; Xu, Y. Enhancement of hydrogen production via methanol steam reforming using a Ni-based catalyst supported by spongy mesoporous alumina. *Green Chem*. **2024,** *26* (9), 5485–5498. DOI: 10.1039/d4gc00397 g.

[20] Wang, I. W.; Kutteri, D. A.; Gao, B.; Tian, H.; Hu, J. Methane Pyrolysis for Carbon Nanotubes and CO x -Free H 2 over Transition-Metal Catalysts. *J. Energy Fuels*. **2019,** *33* (1), 197–205. DOI: 10.1021/acs.energyfuels.8b03502.

[21] Ellison, C.; Lauterbach, J.; Smith, M.W. Activated carbon supported Ni, Fe, and bimetallic NiFe catalysts for COx-free H2 production by microwave methane pyrolysis. *Int. J. Hydrogen Energy*. **2023,** *55* (10), 1062–1070. DOI: 10.1016/J.IJHYDENE.2023.11.150.

[22] Knoks, A.; Grinberga, L.; Sika, R. K.; Vitola, V.; Varnagiris, S.; Urbonavicius, M.; Kleperis J. Investigation of Fe-Ni Catalyst Drying Influence on Methane Pyrolysis for Turquoise Hydrogen Production. *Latv. J. Phys. Tech. Sci*. **2025,** *62* (6), 3–16. DOI: 10.2478/lpts-2025-0041.

[23] Leal Pérez, B.J.; Medrano Jiménez, J.A.; Bhardwaj, R.; Goetheer, E.; van Sint Annaland, M.; Gallucci, F. Methane pyrolysis in a molten gallium bubble column reactor for sustainable hydrogen production: Proof of concept & techno-economic assessment. *Int. J. Hydrogen Energy*. **2021,** *46* (7), 4917–4935. DOI: 10.1016/j.ijhydene.2020.11.079.

[24] Serban, M.; Lewis, M.A.; Marshall, C.L.; Doctor, R. D.. Hydrogen Production by Direct Contact Pyrolysis of Natural Gas. *ACS Energy Fuels*. **2003,** *17* (3), 705–713. DOI: 10.1021/ef020271q.

[25] McConnachie, M.; Konarova, M.; Smart, S. Literature review of the catalytic pyrolysis of methane for hydrogen and carbon production. *Int. J. Hydrogen Energy*. **2023,** *48* (66), 25660–25682. DOI: 10.1016/j.ijhydene.2023.03.123.

[26] Song, J.; Park, S. Review of methane pyrolysis for clean turquoise hydrogen production. *J. Anal. Appl.Pyrolysis*. **2024,** *183*, 106727. DOI: 10.1016/j.jaap.2024.106727.

[27] Prabowo, J.; Lai, L.; Chivers, B.; Burke, D.; Dinh, A. H.; Ye, L.; Wang, Y.; Wang, Y.; Wei, L.; Chen, Y. Solid carbon co-products from hydrogen production by methane pyrolysis: Current understandings and recent progress. *Carbon*. **2024,** *216*. DOI: 10.1016/j.carbon.2023.118507.

[28] Kim, J.; Oh, C.; Oh, H.; Lee, Y.; Seo, H.; Kim, Y. K. Catalytic methane pyrolysis for simultaneous production of hydrogen and graphitic carbon using a ceramic sparger in a molten NiSn alloy. *Carbon*. **2023,** *207*, 1–12. DOI: 10.1016/j.carbon.2023.02.053.

[29] Bayat, N.; Rezaei, M.; Meshkani, F. Methane decomposition over Ni-Fe/Al2O3 catalysts for production of COx-free hydrogen and carbon nanofiber. *Int. J. Hydrogen Energy*. **2016,** *41* (3), 1574–1584. DOI: 10.1016/j.ijhydene.2015.10.053.

[30] Wang, P.; Zhu, H.; Huang, M.; Wan, C.; Li, D.; Jiang, L. Catalytic methane decomposition to hydrogen and carbon over hydrotalcite-derivative composition-uniform and sintering-resistant Ni-Fe/Al2O3 alloy catalysts. *Int. J. Energy Res*. **2022,** *46* (12), 16810–16822. DOI: 10.1002/er.8349.

[31] Al-Fatesh, A. S.; Fakeeha, A. H.; Ibrahim, A. A.; Khan, W. U.; Atia, H.; Eckelt, R.; Seshan, K.; Chowdhury, B. Decomposition of methane over alumina supported Fe and Ni–Fe bimetallic catalyst: Effect of preparation procedure and calcination temperature. *J. Saudi Chem. Soc*. **2018,** *22* (2), 239–247. DOI: 10.1016/j.jscs.2016.05.001.

[32] Angikath, F.; Abdulrahman, F.; Yousry, A.; Das, R.; Saxena, S.; Behar, O.; Alhamed, H.; Altmann, T.; Dally, B.; Sarathy, S.M. Technoeconomic assessment of hydrogen production from natural gas pyrolysis in molten bubble column reactors. *Int. J. Hydrogen Energy*. **2024,** *49*, 246–262. DOI: 10.1016/j.ijhydene.2023.07.308.

[33] Kim, H. S. Techno-economic, exergetic, and life cycle assessment of clean hydrogen production methods using renewable energy: A comparative study of e-methane pyrolysis, e-steam methane reforming, and alkaline water electrolysis. *Int. J. Hydrogen Energy*. **2025,** *100*, 635–645. DOI: 10.1016/j.ijhydene.2024.12.361.

[34] Bolzonella, D.; Battista, F.; Cavinato, C.; Gottardo, M.; Micolucci, F.; Lyberatos, G.; Pavan, P. Recent developments in biohythane production from household food wastes: A review. *Biores Technol*. **2018,** *257*, 311–319. DOI: 10.1016/j.biortech.2018.02.092.

[35] Albayrak, B. *Hydrogen Energy - Challenges and Perspectives*, IntechOpen**2012**. London, UK, ISBN:978-953-51-0812-2.

[36] Makaryan, I. A.; Sedov, I. V.; Salgansky, E. A.; Arutyunov, A. V.; Arutyunov, V. S. A Comprehensive Review on the Prospects of Using Hydrogen–Methane Blends: Challenges and Opportunities. *Energies*. **2022,** *15* (6), 2265. DOI: 10.3390/en15062265.

[37] Anand, A.; Kerketta, A.; Garg, V.K. Moving towards a future of sustainable fuels: A bibliometric approach to global hythane research. *Next Res*. **2025,** *2* (3), 100397. DOI: 10.1016/j.nexres.2025.100397.

[38] Al-Fatesh, A.S.; Abdelkader, A.; Osman, A.I.; Lanre, M.S.; Fakeeha, A.H.; Alhoshan, M.; Alanazi, Y.M.; Awadallah, A.E.; Rooney, D.W. Non-supported bimetallic catalysts of Fe and Co for methane decomposition into H2 and a mixture of graphene nanosheets and carbon nanotubes. *Int. J. Hydrogen Energy*. **2023,** *48* (68), 26506–26517. DOI: 10.1016/j.ijhydene.2022.10.223.

[39] Prabowo, J.; Pan, Y.; Zheng, Z.; Lai, L.; Yang, X.; She, F.; Chen, J.; Liu, F.; Chivers, B.; Wei, L.; Chen, Y. Dual-functional graphitic carbon materials from methane pyrolysis for lithium-ion batteries. *Carbon*. **2025,** *234*, 120038. DOI: 10.1016/j.carbon.2025.120038.

[40] Zhang, J.; Li, X.; Chen, H.; Qi, M.; Zhang, G.; Hu, H.; Ma, X. Hydrogen production by catalytic methane decomposition: Carbon materials as catalysts or catalyst supports. *Int. J, Hydrogen Energy*. **2017,** *42* (31), 19755–19775. DOI: 10.1016/j.ijhydene.2017.06.197.

[41] Otto, M.; Chagoya, K.L.; Blair, R.G.; Hick, S.M.; Kapat, J.S. Optimal hydrogen carrier: Holistic evaluation of hydrogen storage and transportation concepts for power generation, aviation, and transportation. *J. Energy Storage*. **2022,** *55*, 105714. DOI: 10.1016/j.est.2022.105714.

[42] Orozco, F.; Salvatore, A.; Sakulmankongsuk, A.; Gomes, D. R.; Pei, Y.; Araya-Hermosilla, E.; Pucci, A.; Moreno-Villoslada, I.; Picchioni, F.; Bose, R. K. Electroactive performance and cost evaluation of carbon nanotubes and

carbon black as conductive fillers in self-healing shape memory polymers and other composites. *Polymer*. **2022,** *260*, 125365. DOI: 10.1016/j.polymer.2022.125365.

[43] Hantoko, D.; Khan, W. U.; Osman, A. I.; Nasr, M.; Rashwan, A. K.; Gambo, Y.; Al Shoaibi, A.; Chandrasekar, S.; Hossain, M. M. Carbon–neutral hydrogen production by catalytic methane decomposition: a review. *Enviro. Chem. Lett*. **2024,** *22* (4), 1623–1663. DOI: 10.1007/s10311-024-01732-4.

[44] Patzschke, C.F.; Parkinson, B.; Willis, J.J.; Nandi, P.; Love, A.M.; Raman, S.; Hellgardt, K. Co-Mn catalysts for H2 production via methane pyrolysis in molten salts. *Chem. Eng. J*. **2021,** *414*, 128730. DOI: 10.1016/j.cej.2021.128730.

[45] Awadallah, A.E.; Aboul-Enein, A.A.; Kandil, U.F.; Taha, M.R. Facile and large-scale synthesis of high quality few-layered graphene nano-platelets via methane decomposition over unsupported iron family catalysts. *Mater. Chem. Phys*. **2017,** *191*, 75–85. DOI: 10.1016/j.matchemphys.2017.01.007.

[46] Torres, D.; Pinilla, J.L.; Suelves, I. Screening of Ni-Cu bimetallic catalysts for hydrogen and carbon nanofilaments production via catalytic decomposition of methane. *Appl. Catal. A Gen*. **2018,** *559*, 10–19. DOI: 10.1016/j.apcata.2018.04.011.

[47] Zhou, Q.; He, F. Insight into the Mechanism of the Fe-Ni Alloys Co-Deposition from Poly-Nuclear Complexes. *J. Electrochem. Soc*. **2018,** *165* (14), D681–D686. DOI: 10.1149/2.0441814jes.

[48] Yan, P.; Zhang, K.; Peng, Y. Study of Fe2O3-Al2O3 catalyst reduction parameters and conditions for catalytic methane decomposition. *Chem. Eng. Sci*. **2022,** *250*, 117410. DOI: 10.1016/j.ces.2021.117410.

[49] Lee, M. B.; Yang, Q. Y.; Ceyer, S. T. Dynamics of the activated dissociative chemisorption of CH4 and implication for the pressure gap in catalysis: A molecular beam-high resolution electron energy loss study. *J. Chem. Phys*. **1987,** *87* (5), 2724–2741. DOI: 10.1063/1.453060.

[50] Torres, D.; Pinilla, J. L.; Suelves, I. Co-, Cu- and Fe-doped Ni/Al2O3 catalysts for the catalytic decomposition of methane into hydrogen and carbon nanofibers. *Catalysts*. **2018,** *8* (8). DOI: 10.3390/catal8080300.

[51] Hofmann, S.; Csányi, G.; Ferrari, A. C.; Payne, M. C.; Robertson, J. Surface diffusion: The low activation energy path for nanotube growth. *Phys. Rev. Lett*. **2005,** *95* (3), 036101. DOI: 10.1103/PhysRevLett.95.036101.

[52] Ferrari, A. Raman spectroscopy of graphene and graphite: Disorder, electron-phonon coupling, doping and nonadiabatic effects. *Solid State Commun*. **2007,** *143* (1–2), 47–57. DOI: 10.1016/j.ssc.2007.03.052.

[53] Li, Z.; Deng, L.; Kinloch, I. A.; Young, R. J. Raman spectroscopy of carbon materials and their composites: Graphene, nanotubes and fibres. *Progress in Materials Science*. **2023,** *135*, 101089. DOI: 10.1016/j.pmatsci.2023.101089.

[54] Shimada, T.; Sugai, T.; Fantini, C.; et al. Origin of the 2450 cm-1 Raman bands in HOPG, single-wall and double-wall carbon nanotubes. *Carbon*. **2005,** *43* (5), 1049–1054. DOI: 10.1016/j.carbon.2004.11.044.

[55] Pimenta, M. A.; Dresselhaus, G.; Dresselhaus, M. S.; Cançado, L. G.; Jorio, A.; Saito, R. Studying disorder in graphite-based systems by Raman spectroscopy. *Physical Chemistry Chemical Physics*. **2007,** *9* (11), 1276–1291. DOI: 10.1039/b613962k.

[56] Cançado, L. G.; Jorio, A.; Ferreira, E. H. M.; Stavale, F.; Achete, C. A.; Capaz, R. B.; Moutinho, M. V. O.; Lombardo, A.; Kulmala, T. S.; Ferrari, A. C. Quantifying defects in graphene via Raman spectroscopy at different excitation energies. *Nano Lett*. **2011,** *11* (8), 3190–3196. DOI: 10.1021/nl201432 g.

[57] Guzsvány, V. J.; Gaál, F. F.; Bjelica, L. J.; Ökrész, S. N. Voltammetric determination of imidacloprid and thiamethoxam. *J. Serbian Chem. Soc*. **2005,** *70* (5), 735–743. DOI: 10.2298/JSC0505735G.